Faraday Discussions

Cite this: *Faraday Discuss.*, 2023, **244**, 222

PAPER

A comparison of non-covalent interactions in the crystal structures of two σ-alkane complexes of Rh exhibiting contrasting stabilities in the solid state†

M. Arif Sajjad, [a] Stuart A. Macgregor *[a] and Andrew S. Weller [b]

Received 16th January 2023, Accepted 27th January 2023
DOI: 10.1039/d3fd00009e

Non-covalent interactions surrounding the cationic Rh σ-alkane complexes within the crystal structures of $[(Cy_2PCH_2CH_2PCy_2)Rh(NBA)][BAr^F{}_4]$, **[1-NBA][BAr$^F_4$]** (NBA = norbornane, C_7H_{12}; Ar^F = 3,5-$(CF_3)_2C_6H_3$), and **[1-propane][BAr$^F_4$]** are analysed using Quantum Theory of Atoms in Molecules (QTAIM) and Independent Gradient Model approaches, the latter under a Hirshfeld partitioning scheme (IGMH). In both structures the cations reside in an octahedral array of $[BAr^F{}_4]^-$ anions within which the **[1-NBA]$^+$** cation system exhibits a greater number of C–H···F contacts to the anions. QTAIM and IGMH analyses indicate these include the strongest individual atom–atom non-covalent interactions between the cation and the anion in these systems. The IGMH approach highlights the directionality of these C–H···F contacts that contrasts with the more diffuse C–H···π interactions. The accumulative effects of the latter lead to a more significant stabilizing contribution. IGMH $\%\delta G^{atom}$ plots provide a particularly useful visual tool to identify key interactions and highlight the importance of a $-\{C_3H_6\}-$ propylene moiety that is present within both the propane and NBA ligands (the latter as a truncated $-\{C_3H_4\}-$ unit) and the cyclohexyl rings of the phosphine substituents. The potential for this to act as a privileged motif that confers stability on the crystal structures of σ-alkane complexes in the solid-state is discussed. The greater number of C–H···F inter-ion interactions in the **[1-NBA][BAr$^F_4$]** system, coupled with more significant C–H···π interactions are all consistent with greater non-covalent stabilisation around the **[1-NBA]$^+$** cation. This is also supported by larger computed δG^{atom} indices as a measure of cation–anion non-covalent interaction energy.

[a]*Institute of Chemical Sciences, Heriot-Watt University, Edinburgh, EH14 4AS, UK. E-mail: s.a.macgregor@hw.ac.uk*

[b]*Department of Chemistry, University of York, Heslington, York, YO10 5DD, UK*

† Electronic supplementary information (ESI) available: Full computational details and references, computed Cartesian coordinates, tables and images for QTAIM and IGMH calculations. See DOI: **https://doi.org/10.1039/d3fd00009e**

1. Introduction

The development of Solid-state Molecular OrganoMetallic (SMOM) chemistry[1–3] has enabled the study of transition metal σ-alkane complexes by single crystal X-ray diffraction. Such complexes are key intermediates in C–H activation processes,[4–6] but are short-lived in solution even at low temperature.[7] SMOM chemistry exploits gas/solid reactions to effect the single crystal-to-single crystal (SC–SC) transformation of alkene precursor complexes, $[(R_2P(CH_2)_nPR_2)M(alkene)][BAr^F{}_4]$, to the corresponding σ-alkane complexes, $[(R_2P(CH_2)_nPR_2)M(alkane)][BAr^F{}_4]$.[8] Of these $[(Cy_2PCH_2CH_2PCy_2)Rh(NBA)][BAr^F{}_4]$, **[1-NBA][BAr$^F{}_4$]** (NBA = norbornane, C_7H_{12}; $Ar^F = 3,5\text{-}(CF_3)_2C_6H_3$, Scheme 1), is found to be stable for (at least) months under an inert atmosphere and can be synthesized on a gram scale.[9,10] Variation of the bidentate phosphine,[9,11–13] alkene[11,14–16] and counter-anion[12,17] has produced a range of crystallographically characterised Rh and Co[18] σ-alkane complexes that, in conjunction with computational studies,[19] have been shown to exhibit a range of alkane modes that sit along the $\eta^1{}_{C-H}$ (end-on) to $\eta^2{}_{C-H}$ (side-on) continuum.[11]

These σ-alkane complexes also exhibit reactivity in the solid state, including fluxional processes,[10,14,15] H/D exchange reactions[10,15,20] and room temperature alkane dehydrogenation,[15] where these last two categories link σ-alkane complexes directly to a C–H bond activation event. Alkane substitution is also possible; for example, exposure of **[1-NBA][BAr$^F{}_4$]**, to propene gas (Scheme 1) gives **[1-propene][BAr$^F{}_4$]**, in which the Rh–alkene bond is supported by a γ-agostic interaction.[1] Hydrogenation of **[1-propene][BAr$^F{}_4$]** then forms **[1-propane][BAr$^F{}_4$]**, featuring the lightest to date alkane to be characterised crystallographically as a σ-complex.[16] The propane ligand in **[1-propane][BAr$^F{}_4$]** exhibits a 1,3-binding mode with two $\eta^2{}_{C-H} \rightarrow Rh$ interactions that are supported by additional contributions from the geminal C–H bonds.

The microenvironments of the Rh cations within the extended crystal structures of **[1-NBA][BAr$^F{}_4$]** and **[1-propane][BAr$^F{}_4$]** are shown in Fig. 1. In both cases the cation resides in a pseudo-octahedral arrangement of $[BAr^F{}_4]^-$ anions with the σ-alkane ligand sitting within a V-shaped pocket defined by two aryl substituents

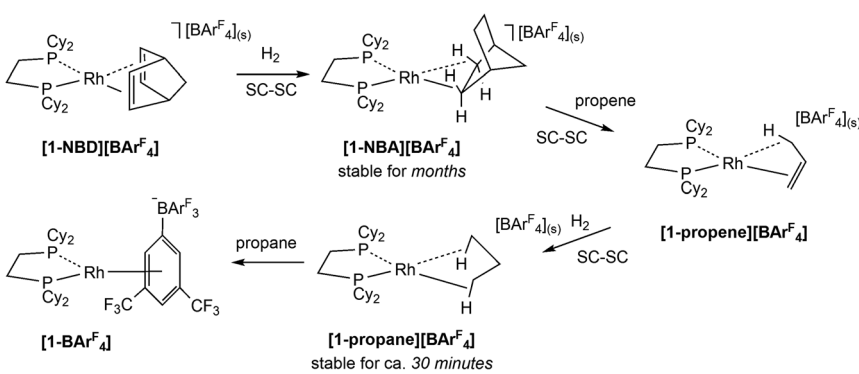

Scheme 1 Synthesis of σ-alkane complexes *via* single crystal-to-single crystal (SC–SC) transformations: (a) **[1-NBA][BAr$^F{}_4$]** by hydrogenation of **[1-NBD][BAr$^F{}_4$]**; (b) **[1-propane][BAr$^F{}_4$]** from **[1-NBA][BAr$^F{}_4$]** *via* sequential NBA/propene substitution and hydrogenation.

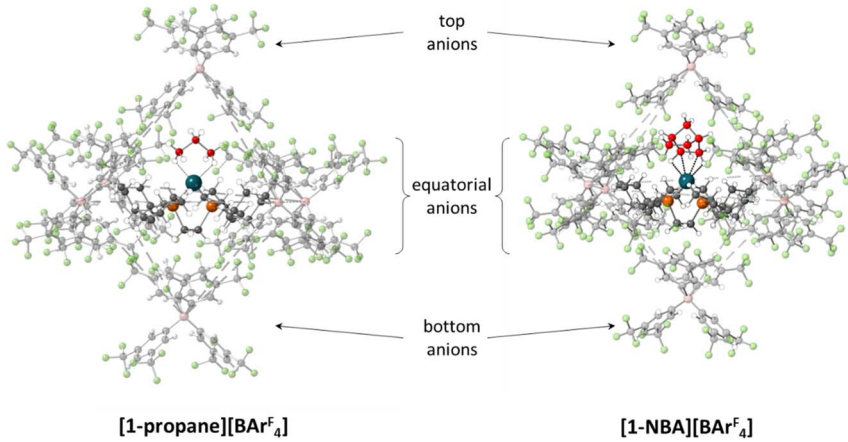

Fig. 1 Packing diagrams showing the pseudo-octahedral arrangement of [BAr$^F_4$]$^-$ anions around the Rh cations in **[1-NBA][BAr$^F_4$]** and **[1-propane][BAr$^F_4$]**. Carbon atoms of the σ-alkane ligands are highlighted in red.

of the adjacent (top) [BAr$^F_4$]$^-$ anion. Despite these similarities, **[1-NBA][BAr$^F_4$]** and **[1-propane][BAr$^F_4$]** show very different behaviours in the solid state: **[1-NBA][BAr$^F_4$]** is stable for months under an inert atmosphere, whereas **[1-propane][BAr$^F_4$]** decomposes within 30 minutes *via* displacement of the alkane by an aryl group of a neighbouring [BAr$^F_4$]$^-$ anion to give zwitterionic **[1-BAr$^F_4$]** (Scheme 1). Indeed, crystallographic characterisation of **[1-propane][BAr$^F_4$]** required the *in situ* hydrogenation of **[1-propene][BAr$^F_4$]** on a synchrotron beamline (Diamond I19) at 150 K.

Understanding the stability of these σ-alkane complexes in the solid-state is a central goal for our research in this area, that aims to exploit SMOM chemistry in catalysis.[1,17] In an early study we showed that computed NBA binding energies across a range of [(R$_2$P(CH$_2$)$_n$PR$_2$)M(alkane)]$^+$ molecular cations (*i.e.* neglecting the effect of the solid-state environment, $n = 2$; R = Cy, ^{i}Bu, ^{i}Pr, O^{i}Pr; $n = 3$, R = ^{i}Pr) showed no correlation with the stability of [(R$_2$P(CH$_2$)$_n$PR$_2$)M(alkane)][BAr$^F_4$] salts in the solid state.[9] Bistoni and co-workers subsequently discussed the role of intramolecular dispersion in the alkane molecular binding energies.[21] However, our subsequent work has shown the importance of including the solid-state environment *via* periodic DFT calculations to achieve reasonable structures and energetics for these σ-alkane complexes.[19] In a recent study, normalised lattice energies, alkane incorporation energies and molecular alkane binding energies were computed for a range of [(Cy$_2$P(CH$_2$)$_2$PCy$_2$)M(alkane)][BAr$^F_4$] complexes (see Fig. 2 for definitions).[16] All three measures were consistent with the greater stability of **[1-NBA][BAr$^F_4$]** over **[1-propane][BAr$^F_4$]**; moreover, a significant, additional stabilization provided by the solid-state environment, ΔE_{SS}, was identified and was larger in **[1-NBA][BAr$^F_4$]** (14.0 kcal mol^{-1} *cf.* 8.3 kcal mol^{-1}).

Previously, non-covalent interactions (NCI) plots[22] have highlighted broad areas of dispersive stabilisation between the alkane ligand and the neighbouring [BAr$^F_4$]$^-$ anions in these σ-alkane complexes.[11,13,14,17,18] In addition, more localised disk-like features have suggested the presence of C–H···F contacts and we have

	Energy/kcal/mol	propane	NBA
[1-alkane][BAr^F_4] $\xrightarrow{\Delta E_{lattice}/Z}$ [1-alkane]$^+$ + [BAr^F_4]$^-$	$\Delta E_{lattice}/Z$	110.4	119.7
[1-alkane]$_Z$[BAr^F_4]$_Z$ $\xrightarrow{\Delta E_{incorp}}$ [1-alkane]$_{Z-1}$[1][BAr^F_4]$_Z$ + alkane	ΔE_{incorp}	34.0	47.1
[1-alkane]$^+$ $\xrightarrow{\Delta E_{molec}}$ [1]$^+$ + alkane	ΔE_{molec}	25.7	33.1
Solid-state stabilization energy ($\Delta E_{SS} = \Delta E_{molec} - \Delta E_{incorp}$)	ΔE_{SS}	8.3	14.0

Fig. 2 Computed normalised lattice energies ($\Delta E_{lattice}/Z$, where Z is the number of formula units in the unit cell), alkane incorporation energies (ΔE_{incorp}) and molecular alkane binding energies (ΔE_{molec}) for **[1-NBA][BAr^F_4]** and **[1-propane][BAr^F_4]**. The solid-state stabilization energy (ΔE_{SS}) is the difference between ΔE_{incorp} and ΔE_{molec}. All values are based on relative SCF energies in kcal mol^{-1} computed with periodic-DFT.

commented on the potential role of such interactions in conferring stability in the solid state.[17] Here we employ Quantum Theory of Atoms in Molecules (QTAIM) and Independent Gradient Model calculations under the recently proposed Hirshfeld partitioning scheme (IGMH[23]) to explore further the role of these non-covalent interactions on the stability of σ-alkane complexes. Our study will focus on the **[1-NBA][BAr^F_4]** and **[1-propane][BAr^F_4]** systems as these exhibit each end of the range of stabilities seen to date in crystallographically characterised σ-alkane complexes in the solid state.

2. Results and discussion

2.1. Methodology

Geometries for **[1-NBA][BAr^F_4]**[9] and **[1-propane][BAr^F_4]**[16] were taken from the reported crystal structures and partially optimised with periodic-DFT calculations at the PBE-D3 level using the CP2K program (see ESI† for full details). B, C, P and Rh atoms were fixed at their experimentally determined positions while H and F atoms were fully relaxed in order to provide reliable H atom positions and to resolve any rotational disorder associated with the CF_3 groups. Unit cell parameters were fixed at the experimental values. Intermolecular interactions were analysed between one central Rh cation and the surrounding pseudo-octahedron of [BAr^F_4]$^-$ anions. Short contacts within crystal structures were analysed with CrystalExplorer[24,25] with van der Waals radii taken from Alvarez (H: 1.20 Å; C: 1.77 Å; F: 1.46 Å).[26] In the following a 'short contact' will refer to a distance at or below the sum of the relevant van der Waals radii. Quantum theory of atoms in molecules (QTAIM[27]) analyses employed the AIMAll program[28] and used the extended wavefunction format. Independent gradient model calculations used Multiwfn[29] and employed the Hirshfeld partitioning scheme (IGMH method).[23] Surfaces were visualised with VMD.[30]

2.2. Geometric analysis of the cation microenvironment

Structures will be analysed in terms of the interaction of the **[1-NBA]$^+$** and **[1-propane]$^+$** cations with the octahedral array of the six surrounding [BAr^F_4]$^-$

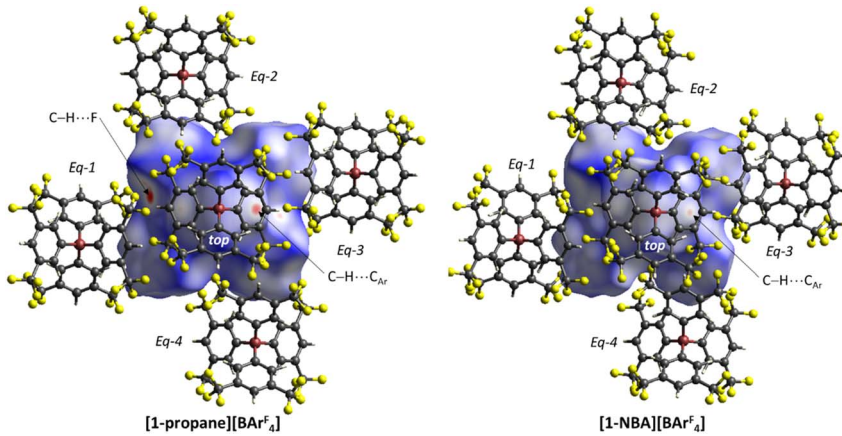

Fig. 3 Hirshfeld surfaces mapped over d_{norm} for **[1-NBA]**$^+$ and **[1-propane]**$^+$ within the octahedral arrays of neighbouring $[BAr^F_4]^-$ anions with the anion labelling system indicated. Views are taken from above the 'top' anion' looking down the $B_{top}\cdots Rh\cdots B_{bottom}$ axis; the 'bottom' anion is obscured by the cation surface.

anions. Fig. 3 displays Hirshfeld surfaces for the **[1-NBA]**$^+$ and **[1-propane]**$^+$ cations within this environment and also defines the anion naming system. The axial direction contains the anions sitting above the alkane (the 'top' anion) and adjacent to the phosphine backbone (the 'bottom' anion) (here obscured by the Hirshfeld surface of the cation as the view is straight down the axial direction). The equatorial anions behave as two distinct pairs, Eq-1 and Eq-3, and Eq-2 and Eq-4, that are distinguished by their alignment with the adjacent phosphine cyclohexyl substituents. Each pair shows a comparable set of non-covalent interactions, as discussed in more detail below. The anion octahedra are slightly compressed with the axial B···B distances somewhat shorter than the *trans*-equatorial B···B distances. Within this the Rh centre sits lower along the axial direction in the NBA complex ($Rh\cdots B_{top} = 9.83$ Å for **[1-NBA][BAr$^F_4$]** and 8.02 Å for **[1-propane][BAr$^F_4$]**), possibly reflecting the larger size of this alkane ligand.

The Hirshfeld surfaces around the alkanes of the **[1-NBA]**$^+$ and **[1-propane]**$^+$ cations are predominantly white and blue indicating that most inter-ion contacts are at or beyond the sum of the van der Waals radii. The red area under the top anion in the **[1-propane][BAr$^F_4$]** system corresponds to a short H···C contact between a Me hydrogen on the propane and a *para*-carbon of the top $[BAr^F_4]^-$. An equivalent but weaker feature in **[1-NBA]**$^+$ involves a bridgehead hydrogen on the NBA. Fingerprint plots indicate that H···F cation–anion contacts are most prevalent in both structures (**[1-NBA][BAr$^F_4$]**: 61.6%; **[1-propane][BAr$^F_4$]**: 63.3%) with H···H and H···C contacts at around 25% and 12% respectively (see Fig. S1–S4† for individual H···X fingerprint plots). A number of H···F short contacts (*i.e.* at or below the sum of the van der Waals radii) are seen and these generally involve cyclohexyl hydrogens rather than the alkane ligands. The intense red spot between the cation and Eq-1 in the Hirshfeld surface of **[1-propane]**$^+$ is an example of this and corresponds to a short H···F contact of 2.22 Å.

More detail on the distribution of C–H···F contacts around the **[1-NBA]**$^+$ and **[1-propane]**$^+$ cations that are below 3.0 Å is provided in the scatterplots in Fig. 4.

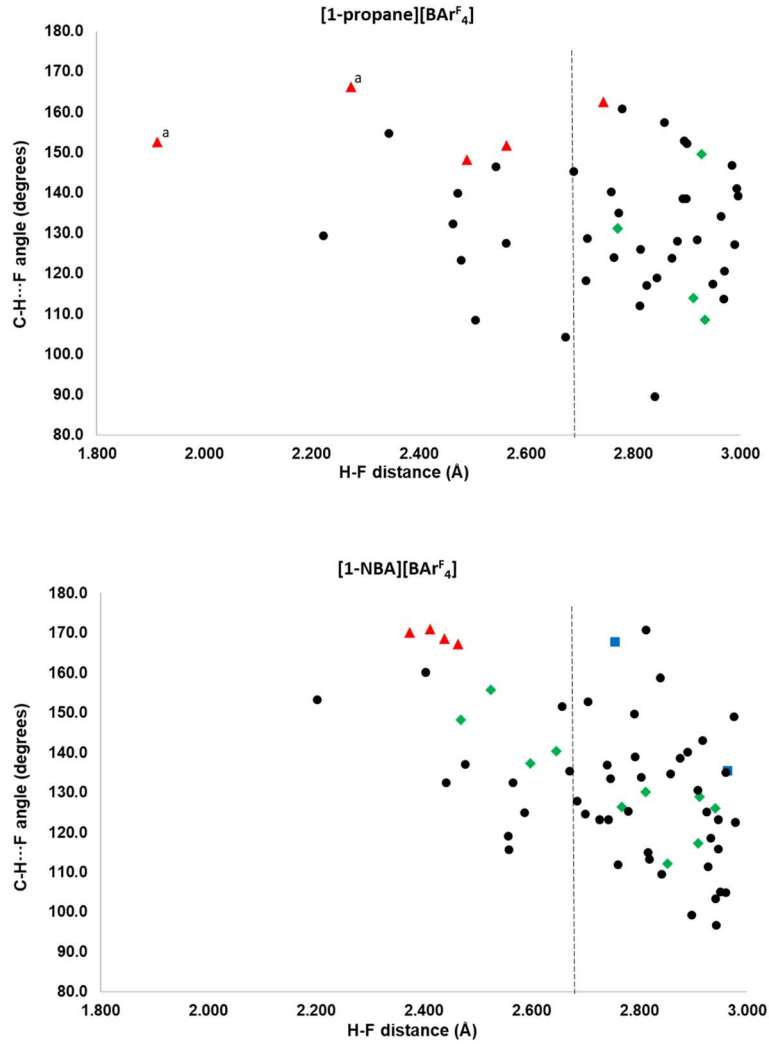

Fig. 4 Scatterplots of H···F distance (Å) *vs.* C–H···F angle (degrees) for the **[1-NBA]**$^+$ and **[1-propane]**$^+$ cations within the octahedral arrays of neighbouring $[BAr^F_4]^-$ anions. The dashed vertical line indicates the sum of the van der Waals radii for H and F. [a]Data points correspond to two equivalent H···F contacts.

Three classes of cation–anion contacts are seen: (i) alkane C–H···F (in green); (ii) phosphine backbone C–H···F (blue) and (iii) phosphine cyclohexyl C–H···F contacts (black). In addition a small number of anion–anion C–H···F contacts are shown in red. The cyclohexyl C–H···F contacts are most common and are more numerous for **[1-NBA]**$^+$ than **[1-propane]**$^+$ (45 compared to 36). There are no cyclohexyl C–H···F contacts to the top anion in either structure. No correlation between H···F distance and C–H···F angle is seen, beyond the absence of short H···F contacts with low C–H···F angles. **[1-NBA]**$^+$ features two C–H···F contacts from the phosphine backbone while no such contacts are seen around **[1-propane]**$^+$. Of the inter-anion C–H···F contacts in red (four in **[(1-NBA)][BAr$^F_4$]** and

seven in **[1-propane][BAr$^F_4$]**) all but one is a short contact, and these are also among the closest to linear (150–170°). These features have been taken as evidence for C–H···F H-bonding[31–33] and this could be promoted by the relative acidity of the C–H H-bond donors that are located between two CF_3 substituents on the aryl rings. A more detailed discussion of the role of these inter-anion contacts will be the subject of a separate study.

Comparing the alkane ligands, in **[1-propane]$^+$** the propane displays four C–H···F contacts below 3.0 Å, although none is below the sum of the van der Waals radii. The NBA in **[1-NBA]$^+$** has 10 C–H···F contacts, four of which are short contacts. A general trend towards wider C–H···F angles with shorter H···F distances can be seen in the alkane C–H···F data for **[1-NBA][BAr$^F_4$]** and this is similar to the data in Boese, Nangia and Desiraju's early study on fluorobenzenes, where C–H···F H-bonding was proposed especially when more acidic C–H bonds are present.[32] This is discussed in the context of the present systems after these C–H···F contacts have been considered in more detail *via* electronic structure analyses.

2.3. Electronic structure analyses

QTAIM molecular graphs were computed for all six cation–anion ion-pairs that can be formed within the **[1-NBA][BAr$^F_4$]** and **[1-propane][BAr$^F_4$]** 'octahedra' – *i.e.* where the central cation is common to all six ion-pairs and is treated in turn with each adjacent anion. The range of C–H···F, C–H···C_{aryl} and C–H···H_{aryl} bond paths characterised are summarised in Table 1. Individual bond critical point (BCP) metrics are listed in the ESI (see Fig. S5–S16†). The C–H···F bond paths are most numerous, there being almost twice as many of these as the total of C–H···C_{aryl} and C–H···H_{aryl} bond paths. Overall the **[1-NBA]$^+$** cation exhibits significantly more bond paths to the surrounding anions (88 *cf.* 72 around **[1-propane]$^+$**) and this is primarily due to a greater number of C–H···F bond paths (61 *cf.* 46).

2.3.1. The top ion-pairs. The propane ligand in **[1-propane][BAr$^F_4$]** exhibits 10 bond paths in total (four C–H···F and six C–H···C_{aryl}) compared to 14 around the NBA in **[1-NBA][BAr$^F_4$]** (nine C–H···F and five C–H···C_{aryl}). In both cases all but two of these involve the top anion and molecular graphs for these ion-pairs are compared in Fig. 5. For the **[1-propane][BAr$^F_4$]** top ion-pair the C_1–H_{11}···F_{11} and C_1–H_{11}···F_{12} bond paths correspond to two of the four C–H···F contacts noted above (the remaining two contacts are to equatorial anions, see below). In contrast, the equivalent C_3–H_{31}···$F_{21/22}$ distances exceed 3.30 Å and no bond path is seen. H_{11} and H_{31} also exhibit bond paths and short contacts to the *para*-carbons on the adjacent Ar^F groups (C_{1para} and C_{2para}): these have the largest bond critical point BCP electron densities in this ion-pair (C_1–H_{11}···C_{1para} = 2.52 Å, $\rho(r) = 10.3 \times 10^{-3}$ a.u.; C_3–H_{31}···C_{2para} = 2.67 Å, $\rho(r) = 7.8 \times 10^{-3}$ a.u.) and correspond to the red feature beneath the top anion noted previously in the Hirshfeld surfaces. The four C–H···C_{aryl} bond paths involving H_{21} and H_{22} on the central methylene correspond to long contacts (>3.25 Å; $\rho(r) < 3.2 \times 10^{-3}$ a.u.).

Within the **[1-NBA][BAr$^F_4$]** ion-pair the –{C_3H_4}– moiety comprising the bridgehead (C_3–H_3 and C_6–H_6) and central bridging methylene (C_7–H_{71}/C_7–H_{72}) bonds behaves as a "propane" fragment and forms two C–H···F and five C–H···C_{aryl} bond paths that are equivalent to similar bond paths in **[1-propane][BAr$^F_4$]**. Consistent with this, the highest $\rho(r)$ values within this set are for the C_3–H_3···

Table 1 Summary of bond paths around the cations in [1-NBA][BAr^F_4] and [1-propane][BAr^F_4]

		[1-Propane][BAr^F_4]		[1-NBA][BAr^F_4]	
Anion	Bond path	Number[a]	$\rho(r)$/a.u. $\times 10^{-3}$	Number	$\rho(r)$/a.u. $\times 10^{-3}$
Top	C–H···F	2	3.3, 3.3	7	2.6–7.7
	C–H···C	6	2.8–10.3	5	4.1–7.7
Eq-1	C–H···F	8 (5/2/1)	2.2–14.1	12 (7/4/1)	2.0–8.8
	C–H···C	4[b]	2.0–4.4	3	2.7–5.4
	C–H···H	1	3.5	3	3.9–5.8
Eq-2	C–H···F	10 (5/4/1)	1.2–8.2	12 (7/4/1[b])	1.3–6.9
	C–H···C	3	1.9–4.4	2	4.0, 4.7
	C–H···H	2	4.5, 5.0	2	6.6, 7.9
Eq-3	C–H···F	7 (4/3)	1.2–4.5	10 (5/4/1)	2.4–9.1
	C–H···C	2	3.6, 5.6	2[b]	3.7, 4.4
	C–H···H	2	3.2, 5.6	2	5.2, 5.4
Eq-4	C–H···F	9 (5/4)	1.5–8.2	9 (3/4/2)	2.6–7.9
	C–H···C	2	4.6, 7.0	2	3.1, 3.4
	C–H···H	2	4.2, 6.4	2	3.8, 10.2
Bottom	C–H···F	10	1.5–10.5	11	1.8–13.0
	C–H···C	2	1.3, 1.4	3	2.0–3.5
	C–H···H	—		1	2.1
Total	C–H···F	46 (29[c]/13/4)	1.2–14.1	61 (33[c]/16/12)	1.3–13.0
	C–H···C	19	1.9–10.3	17	2.0–5.4
	C–H···H	7	3.2–6.4	10	2.1–10.2

[a] Values in parentheses indicate the number of C–H···F bond paths involving the cyclohexyl substituents within the conical pocket of anion aryl groups (Cy_{inner}), the cyclohexyl outside that pocket (Cy_{outer}) and, where appropriate, the alkane ligand, respectively (see text for details). [b] One C···F bond path is also present; see ESI for details. [c] Includes C–H···F bond paths from the $-C_2H_4-$ backbone of the diphosphine ligand.

C_{2para} and C_6–H_6···C_{1para} bond paths ($\rho(r) = 5.9 \times 10^{-3}$ and 7.7×10^{-3} a.u.). The NBA system has additional bond paths from both pairs of *exo*-C–H bonds. Of these the C_4–H_{42}···F_{21} and C_5–H_{52}···F_{11} bond paths correspond to the two shortest C–H···F contacts (2.47 Å and 2.53 Å) and have higher $\rho(r)$ values (7.7×10^{-3} a.u. and 6.7×10^{-3} a.u.). The C_1–H_{12}···F_{12} and C_2–H_{22}···F_{22} bond paths are weaker, with longer contacts (2.77 Å and 2.94 Å) and lower $\rho(r)$ (3.6×10^{-3} a.u. and 2.4×10^{-3} a.u.). The final additional feature of the NBA system is a weak C_7–H_{72}···F_{22} bond path (3.02 Å; $\rho(r) = 2.6 \times 10^{-3}$ a.u.).

In general, the C–H···F BCP metrics computed here are similar to those reported in previous studies of C–H···F contacts and show an exponential relationship between the H···F distance and $\rho(r)$ (see Fig. S26†).[34–36] Such interactions have been ascribed weak H-bonding character that is enhanced by a more acidic C–H bond.[32,33] An electron deficient cationic Rh(I) centre could enhance such interactions *via* polarization of both the *endo*-C–H bonds directly involved in the

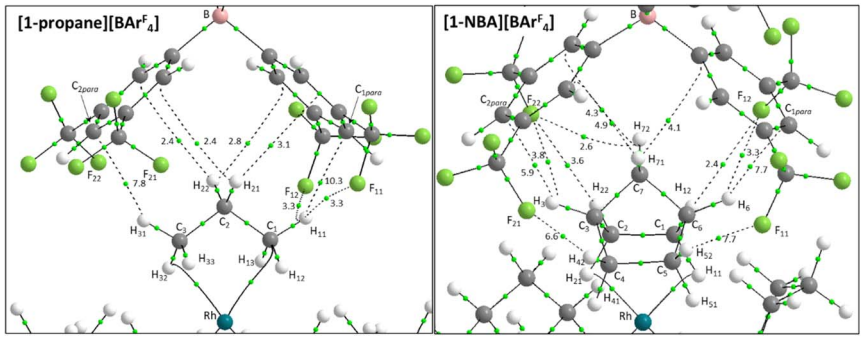

Fig. 5 QTAIM molecular graphs for the top ion-pairs in **[1-propane][BAr$^F_4$]** and **[1-NBA][BAr$^F_4$]**, with bond critical bonds (BCPs) in green and selected BCP electron densities, $\rho(r)$, indicated in a.u. $\times 10^{-3}$. Bond paths with $\rho(r) < 0.001$ a.u., intramolecular bond paths and ring critical points (RCP) are omitted for clarity.

σ-interaction and, through induction effects, the geminal *exo*-C–H bonds and beyond.[37] To assess this, the molecular graphs in Fig. 5 were recomputed with the $\{(Cy_2P(CH_2)_2PCy_2)Rh\}^+$ fragments removed. Computed QTAIM charges confirmed the alkane hydrogen atoms do indeed become more positively charged when the alkane are bound to Rh, however, the same networks of bond paths with virtually unchanged BCP metrics were seen (see Fig. S25†). This lack of influence of the Rh fragment implies at best weak H-bonding character in these C–H···F interactions.

The C–H···C_{aryl} bond paths (six around **[1-propane]$^+$**, five around **[1-NBA]$^+$**) suggest the presence of C–H···π type interactions in both ion-pairs.[38–41] Previously, NCI plots have highlighted broad areas of dispersive stabilisation between σ-bound alkanes and the adjacent anions.[11,13,14,17,18] Here, we have used the Independent Gradient Model (IGM) approach[42,43] to isolate non-covalent interactions between the cation and anion. This method is based on atomic electron densities and uses the descriptor, δG, the difference in the upper limit of the electron density gradient of the non-interacting system *vs.* the electron density gradient of the interacting system. Here the Hirshfeld partitioning scheme of the molecular electron density proposed by Lu and Chen (and implemented within Multiwfn) is employed to define the atomic electron densities (IGMH approach).[23] The results of these IGMH analyses for the top ion-pairs are displayed in Fig. 6, both as isosurfaces of δG^{inter} and as colour-coded $\%\delta G^{atom}$ scores that highlight the atoms that contribute most significantly to these inter-ion interactions. These $\%\delta G^{atom}$ scores are the sum of all the interactions of a given atom on the cation with all the atoms of the anion; individual atom–atom interactions can also be quantified as δG^{atom} indices.

The IGMH isosurfaces amplify the features seen in the QTAIM molecular plots. For **[1-NBA][BAr$^F_4$]** distinct disk-like features consistent with *exo*-C–H···F contacts are seen and these are much more pronounced than in **[1-propane][BAr$^F_4$]**. The peripheral alkane C–H···C_{para} (anion) contacts are also common to both structures, but these are more extensive in **[1-NBA][BAr$^F_4$]**. This is confirmed by the % δG^{atom} values, where the relative contribution of each atom is represented on a blue–green–red scale (blue: zero; red: the maximum contribution, see also inset for % atomic contributions in the cations). The strongest contributions in **[1-NBA]**

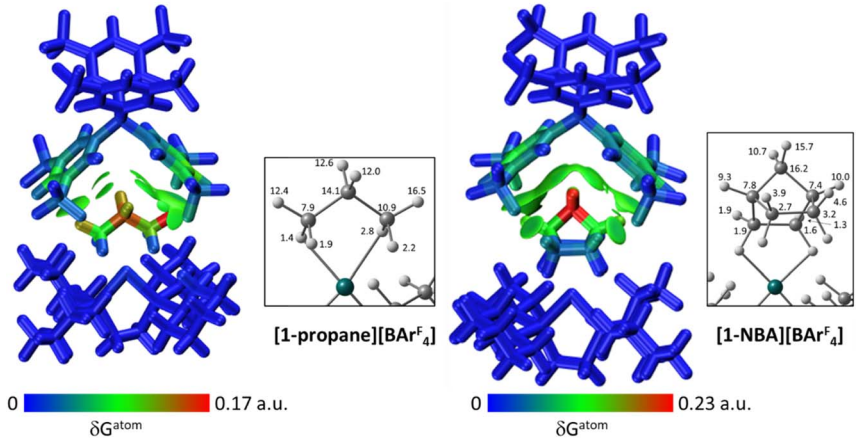

Fig. 6 IGMH plots for the **[1-NBA][BAr$^F_4$]** and **[1-propane][BAr$^F_4$]** top ion-pairs where the cations and anions are defined as separate fragments. Sign(λ_2)ρ-coloured isosurfaces are plotted with δG^{inter} = 0.003 a.u. and atoms are coloured by $\%\delta G^{atom}$ to highlight their relative contributions. The insets show all $\%\delta G^{atom}$ contributions on the cations that are above 1%.

[BAr$^F_4$] are associated with the bridging methylene (C_7, H_{71} and H_{72}) whereas H_{31} is most prominent in **[1-propane][BAr$^F_4$]**. The atoms involved in the *exo*-C–H···F contacts show little lightening of the blue colour, indicating a minimal contribution. This is confirmed by the $\%\delta G^{atom}$ values: the bridgehead and bridging methylene atoms that make up the –{C_3H_4}– "propane" fragment within the NBA ligand account for 77.0% of the total interaction, whereas the *exo*-hydrogen atoms, H_{42} and H_{52}, that are involved in H···F short contacts contribute only 4.6% and 3.9% respectively. The δG^{atom} indices, that quantify individual atom–atom contributions, show that the $H_{42}\cdots F_{21}$ and $H_{52}\cdots F_{11}$ pairs are ranked 2nd and 4th strongest (1.8% and 1.7%) and are comparable in strength to the $H_3\cdots C_{2para}$ and $H_6\cdots C_{1para}$ pairs (1.9% and 1.8%, see Fig. S11†). These data are also consistent with the similar BCP $\rho(r)$ values computed for the equivalent bond paths. However, H_{42} and H_{52} engage in relatively few additional atom–atom contacts whereas all atoms in the –{C_3H_4}– "propane" moiety have numerous atom–atom contributions that accumulate to make them more significant in the inter-fragment interaction. This difference between the directional C–H···F contacts and the more diffuse C–H···C_{aryl} contacts is a recurring theme in this study. For **[1-propane][BAr$^F_4$]** the equivalent –{C_3H_4}– moiety accounts for 87.0% of the total interaction, but of this only 3.4% is due to $H_{11}\cdots F_{11}$ and $H_{31}\cdots F_{22}$ atom–atom contributions.

Overall, the alkane ligands dominate the cation component to the non-covalent interactions in these ion-pairs: summing $\%\delta G^{atom}$ values from all atoms of the propane ligand accounts for 94.6% of the interaction while for the NBA ligand the equivalent sum gives 99.5%. These values are summarised in Table 2, where comparison with the other ion-pairs studied below is also made. Also included in Table 2 are the sum of the individual δG^{atom} indices. These give an indication of the accumulative strength of the non-covalent interactions

Table 2 % Contributions for the cations fragments indicated within the six ion-pairs in **[1-propane][BAr$^F_4$]** and **[1-NBA][BAr$^F_4$]**. δG^{atom} indices (a.u.) are summed for all atom pairs across each ion-pair

	[1-Propane][BAr$^F_4$]		**[1-NBA][BAr$^F_4$]**	
Ion-pair	% Contribution	$\Sigma\delta G^{atom}$ index	% Contribution	$\Sigma\delta G^{atom}$ index
Top	**Propane**		**NBA**	
	94.6	0.95	99.5	1.39
Equatorial	**Cy$_{inner}$/Cy$_{outer}$/propane**		**Cy$_{inner}$/Cy$_{outer}$/NBA**	
Eq-1	76.0/21.0/2.4	1.14	75.3/20.2/3.8	1.50
Eq-2	83.6/14.9/1.1	0.82	69.3/18.5/11.7	1.24
Eq-3	80.0/16.0/3.3	1.19	82.8/13.2/3.2	1.38
Eq-4	86.4/12.1/1.1	1.05	72.9/15.4/10.5	1.10
Bottom	**Cy$_{1-4}$/C$_2$ backbone**		**Cy$_{1-4}$/C$_2$ backbone**	
	74.9/24.2	0.87	69.0/29.1	1.13

between the cation and anion and show higher values for **[1-NBA][BAr$^F_4$]** over **[1-propane][BAr$^F_4$]** (for the top anion 1.39 *vs.* 0.95).

2.3.2. 'Equatorial' ion-pairs. The data in Table 1 show all four equatorial ion-pairs feature more C–H···F bond paths than around the alkanes in the top ion-pairs', and that these are greater in number around **[1-NBA]$^+$** than around **[1-propane]$^+$**. Both alkanes show one C–H···F bond path to each of the Eq-1 and Eq-3 anions that arise from terminal hydrogen atoms within the "propane" moieties (*i.e.* H_{11} and H_{31} in **[1-propane]$^+$** and H_3 and H_6 in **[1-NBA]$^+$**), although these have $\rho(r)$ values below 3.2×10^{-3} a.u. The H_{41} and H_{51} *exo*-hydrogens in **[1-NBA]$^+$** contribute an additional three bond paths, two of which equate to short contacts (2.60 Å, $\rho(r) = 5.8 \times 10^{-3}$ a.u.; 2.65 Å, $\rho(r) = 4.9 \times 10^{-3}$ a.u.). All the remaining C–H···F bond paths involve cyclohexyl hydrogens. These equatorial ion-pairs also feature several C–H···C$_{aryl}$ bond paths and C–H···H$_{aryl}$ bond paths, the latter always to *ortho* ring H atoms.

The molecular graph for the ion-pair with Eq-1 in **[1-propane][BAr$^F_4$]** is shown in Fig. 7(a). This displays a pattern, common to all these ion-pairs, in which one cyclohexyl substituent (Cy$_{inner}$, here Cy$_1$) sits within a conical pocket defined by three of the anion aryl groups (Ar$^F_{eq11}$, Ar$^F_{eq12}$ and Ar$^F_{eq13}$) while a second cyclohexyl substituent (Cy$_{outer}$, here Cy$_2$) sits outside this pocket. The former displays a range of C–H···F, C–H···C$_{aryl}$ and C–H···H$_{aryl}$ bond paths while the latter only exhibits C–H···F bond paths. In the Eq-1 ion-pair Cy$_1$ lies approximately parallel to the aromatic ring of Ar$^F_{eq11}$ and shows five C–H···F bond paths that are distributed across all three Ar^F groups of the pocket. In contrast the C–H···C$_{aryl}$ bond paths are all directed to carbons on Ar$^F_{eq11}$ and the shortest of these involves the C3-axial hydrogen and an *ortho* ring-carbon ($H_{Cy131}\cdots C_{eq112}$ = 3.06 Å; $\rho(r) = 4.2 \times 10^{-3}$ a.u.). All these bond paths have low $\rho(r)$ values below 4.2×10^{-3} a.u. In contrast, the C3-equatorial hydrogen, H_{Cy132}, is directed away from Ar$^F_{eq11}$ and engages in two C–H···F bond paths ($\rho(r) = 2.0 \times 10^{-3}$ a.u. and 3.4×10^{-3} a.u.) and one C–H···H$_{aryl}$ bond path to H_{eq121} ($\rho(r) = 3.5 \times 10^{-3}$ a.u.). Cy$_2$ exhibits two C–H···F bond paths, one of which has a very short contact ($H_{Cy222}\cdots F_{eq112}$ = 2.22 Å) and the highest $\rho(r)$ value of 14.1×10^{-3} a.u. within this ion-pair

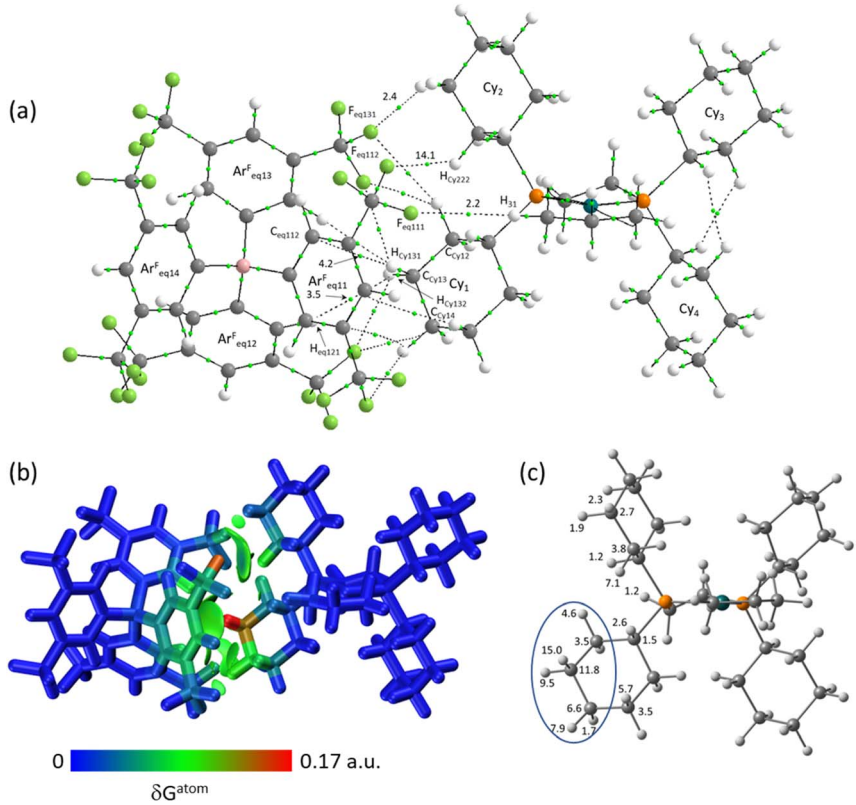

Fig. 7 (a) QTAIM molecular graph for the Eq-1 ion-pair in **[1-propane][BAr$^F_4$]** with BCPs in green and showing selected atom labels and BCP electron densities (a.u. $\times$ 10^{-3}). Bond paths with $\rho(r) < 0.001$ a.u., intramolecular bond paths and ring critical points (RCP) are omitted for clarity. (b) IGMH plot where the cation and anion are defined as separate fragments. Sign(λ_2)ρ-coloured isosurfaces are plotted with $\delta G^{inter} = 0.003$ a.u. and atoms are coloured by $\%\delta G^{atom}$. (c) $\%\delta G^{atom}$ contributions on the cation that are above 1%, with the propylene motif highlighted (see text for details).

and indeed across both systems. This corresponds to the intense red C–H···F short contact noted on the Hirshfeld surface in Fig. 3 beside Eq-1.

These different interactions are reflected in the IGMH isosurfaces in Fig. 7(b). The C–H···F interactions from Cy_2 can be clearly seen with the darker green region equating to the short $H_{Cy222}\cdots F_{eq112}$ contact noted above. The orange colour of F_{eq112} in the $\%\delta G^{atom}$ colouring confirms a significant contribution from that atom: the $H_{Cy222}\cdots F_{eq112}$ pair also has the single largest atom–atom δG^{atom} index at 4.1%. More significant, however, is the green isosurface between Cy_1 and Ar^F_{eq11}. In this case the $\%\delta G^{atom}$ colouring highlights the C3-axial hydrogen, H_{Cy131}, in red, indicating the largest single atomic contribution (15.0%). The C3-equatorial hydrogen contributes 9.5% – somewhat lower as it is engaged in more directional C–H···F interactions. More generally, the cation interaction is dominated by the –{C_3H_6}– propylene motif centred on the C_{Cy12}, C_{Cy13} and C_{Cy14} carbons and ringed in Fig. 7(c). Together these atoms contribute 62.9% of the interaction from the cation.

Within the other equatorial ion-pairs a similar pattern of bond paths is seen, with BCP $\rho(r)$ values generally between 1.0 and 6.0 $\times$ 10^{-3} a.u. Any bond paths with higher BCP $\rho(r)$ values all correspond to short contacts below the sum of the relevant van der Waals radii: there are four such C–H$\cdots$F, two C–H$\cdots C_{aryl}$ and one C–H$\cdots C_{aryl}$ bond paths, within which the highest $\rho(r)$ value is 8.2 $\times$ 10^{-3} a.u. Of the three remaining equatorial ion-pairs Eq-3 behaves like Eq-1 with one Cy group lying side-on within the conical pocket and the equivalent –{C_3H_6}– propylene motif centred on the C3 methylene group and contributing 62.0% of the cation interaction. With Eq-2 and Eq-4 the inner cyclohexyl groups (Cy_2 and Cy_4, respectively) show a more end-on geometry within the pocket (see Fig. 8 for the ion-pair with Eq-2). As a result, both the equatorial and axial hydrogens of the C4 atom (H_{Cy241} and H_{Cy242}) engage in C–H$\cdots C_{aryl}$ bond paths and this is most clearly seen when visualised as $\%\delta G^{atom}$ in the IGMH plot. This methylene group alone accounts for 49.6% of the cation interaction with Eq-2 and this increases to 76.9% when expanded to include the neighbouring CH_2 groups (circled in Fig. 8(c)).

The four equatorial ion-pairs in the **[1-NBA][BAr$^F_4$]** system exhibit the same general geometric pattern as in **[1-propane][BAr$^F_4$]** with each ion-pair having one inner cyclohexyl group, Cy_{inner}, within the $[BAr^F_4]^-$ conical pocket and one outer Cy group, Cy_{outer}, outside that pocket. Geometrically the Eq-1/Eq-3 and Eq-2/Eq-4 ion-pairs again form distinct pairs, with the Cy_{inner} groups being more side-on in the former and interacting primarily through a propylene motif centred on the C3 methylene, while in the latter the Cy_{inner} groups are more end-on and interact most strongly *via* the propylene motif centred on the C4 methylene. QTAIM molecular graphs, IGMH isosurfaces and $\%\delta G^{atom}$ plots for all ion-pairs are provided in the ESI (see Fig. S18–S25†).

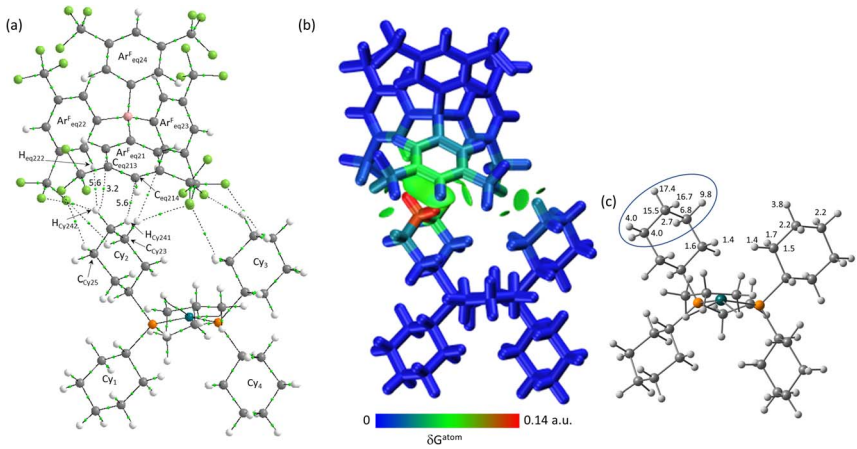

Fig. 8 (a) QTAIM molecular graph with Eq-2 in **[1-propane][BAr$^F_4$]** with BCPs in green and showing selected atoms and BCP electron densities (a.u. $\times$ 10^{-3}). Bond paths with $\rho(r)$ < 0.001 a.u., intramolecular bond paths and ring critical points (RCP) are omitted for clarity. (b) IGMH plot where the cation and anion are defined as separate fragments. Sign(λ_2)ρ-coloured isosurfaces are plotted with δG^{inter} = 0.003 a.u. and atoms are coloured by δG^{atom}. (c) $\%\delta G^{atom}$ contributions on the cation that are above 1%, with the propylene motif highlighted (see text for details).

Table 2 compares the data for the equatorial ion-pairs in **[1-propane][BAr$^{F}_{4}$]** and **[1-NBA][BAr$^{F}_{4}$]**. Here the %δG^{atom} data have been summed over all atoms of three fragments within the cations: Cy_{inner}, Cy_{outer} and the alkane ligand. In each case Cy_{inner} dominates and a very similar distribution is seen for the Eq-1 and Eq-3 ion-pairs in both systems. The contribution from the alkane ligand is very small (<4%). In contrast, the Eq-2/Eq-4 ion-pairs differ significantly between the two systems: in **[1-propane][BAr$^{F}_{4}$]** Cy_{inner} contributes 83.6% and 86.4% respectively, whereas this drops to 69.3% and 72.9% in **[1-NBA][BAr$^{F}_{4}$]**. The major reason for this is a relatively more significant contribution from the NBA ligand (*ca.* 11% *cf.* 1% in **[1-propane][BAr$^{F}_{4}$]**). In all cases the strength of the non-covalent interactions between the cation and the anions, as gauged by the sum of δG^{atom} indices, is significantly greater for **[1-NBA][BAr$^{F}_{4}$]**.

2.3.3. Bottom ion-pairs. The QTAIM molecular graph, IGMH isosurface and δG^{atom} plot for the bottom ion-pair in the **[1-propane][BAr$^{F}_{4}$]** system are shown in Fig. 9. In this case each of the cyclohexyl substituents, Cy_1–Cy_4, sits above a CF_3 group on the $[BAr^{F}_{4}]^{-}$ anion. C–H···F bond paths therefore dominate and of the 10 of these, three equate to short H···F contacts from axial hydrogen atoms on Cy_1, Cy_2 and Cy_3, for which $\rho(r)$ values are provided in Fig. 9(a). The $-C_2H_4-$ ethylene backbone of the diphosphine ligand also contributes two C–H···C_{aryl} bond paths, albeit with $\rho(r)$ values below 2×10^{-3} a.u. In terms of the cation %

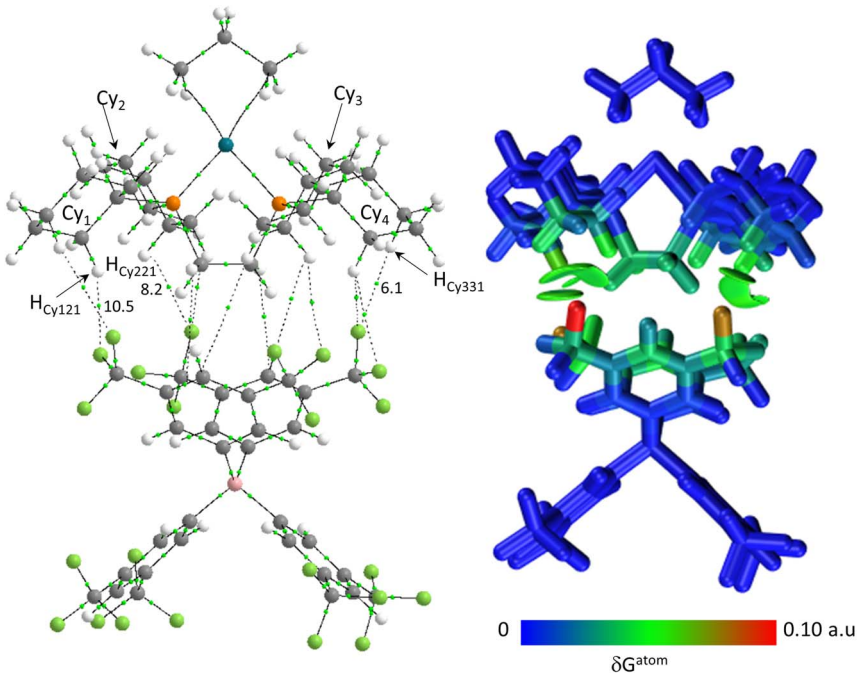

Fig. 9 (a) QTAIM molecular graph with the bottom anion in **[1-propane][BAr$^{F}_{4}$]** with BCPs in green and showing selected atoms and BCP electron densities (a.u. $\times 10^{-3}$). Bond paths with $\rho(r) < 0.001$ a.u., intramolecular bond paths and ring critical points (RCP) are omitted for clarity. (b) IGMH plot where the cation and anion are defined as separate fragments. Sign(λ_2)ρ-coloured isosurfaces are plotted with $\delta G^{inter} = 0.003$ a.u. and atoms are coloured by δG^{atom}.

fragment contributions (Table 2), the cyclohexyl groups total 74.9% and this is distributed approximately evenly over all four substituents. The $-C_2H_4-$ backbone also contributes significantly (24.2%), despite there only being two weak bond paths from this fragment. The equivalent ion-pair in **[1-NBA][BAr$^F_4$]** displays eleven C–H···F bond paths, two of which correspond to short contacts; one of these has an H···F distance of 2.20 Å and a relatively high $\rho(r)$ value of 13.0×10^{-3} a.u., and is one of the shortest contacts in either system (see Fig. S16†). The % fragment contributions are now slightly shifted toward the $-C_2H_4-$ backbone. As with the other ion-pairs the $\Sigma\delta G^{atom}$ index value is larger for the **[1-NBA][BAr$^F_4$]** system.

2.4. Discussion

A combination of geometric and electronic structure analyses have revealed significant differences in the non-covalent interactions around the Rh cations in the σ-alkane complexes **[1-propane][BAr$^F_4$]** and **[1-NBA][BAr$^F_4$]**. The NBA system exhibits more C–H···F short contacts and bond paths and the NBA ligand contributes more significantly to inter-ion interactions, not only in the top anion where the alkanes dominate, but also in two of the equatorial anions (Eq-2 and Eq-4). $\Sigma\delta G^{atom}$ indices are higher for all the cation–anion ion-pairs in the NBA system. These data are all consistent with previous work that quantified an additional stabilisation in **[1-NBA][BAr$^F_4$]** that was due to the solid-state environment (5.7 kcal mol^{-1}, Fig. 2).[16] However, what precisely is the driving force that creates this greater stability and what role does it play, if any, in determining the chemical stability of these crystalline solids?

The presence of several propylene motifs in the cations, either from the propane ligand itself, the cyclohexyl substituents or, for the NBA ligand, a topologically related $-\{C_3H_4\}-$ moiety, is a recurring pattern in all but the bottom ion-pairs. While this does not discriminate the **[1-propane][BAr$^F_4$]** and **[1-NBA][BAr$^F_4$]** systems (with their very different chemical stability) it may be that this propylene moiety acts as a privileged motif for the formation of σ-alkane complexes in the solid state, providing a robust environment such that these species are long-lived after the SC–SC transformations necessary for their formation. Other closely related NBA complexes, $[(R_2PCH_2CH_2PR_2)Rh(NBA)][BAr^F_4]$, that lack the rigid propylene motif of the cyclohexyl substituents show very different behaviours: with R = ^{i}Bu[8] the system is only stable for a few hours at room temperature whereas with R = ^{i}OPr[9] the corresponding alkane complex cannot be isolated and the formation of the zwitterion **[1-BAr$^F_4$]** is observed. The combination of the cyclohexyl substituents and the NBA ligand is clearly particularly favourable.

A further indication of the importance of the propylene motif is seen with the cyclopentyl (Cyp) analogue, $[(Cyp_2PCH_2CH_2PCyp_2)Rh(NBA)][BAr^F_4]$, **[2-NBA][BAr$^F_4$]**.[44] With **[1-NBA][BAr$^F_4$]** hydrogenation of the NBD precursor proceeds with rotation of the NBA ligand such that the plane of the C7 bridging methylene is perpendicular to the {PRhP} coordination plane (see Fig. 10 and Scheme 1). Remarkably, with **[2-NBA][BAr$^F_4$]** the NBA ligand is stationary and it is the $\{Rh(Cyp_2CH_2CH_2PCyp_2)\}^+$ fragment that rotates. Thus the excision of a single methylene group from each of the phosphine substituents significantly perturbs the behaviour of the system in the SC–SC transformation.

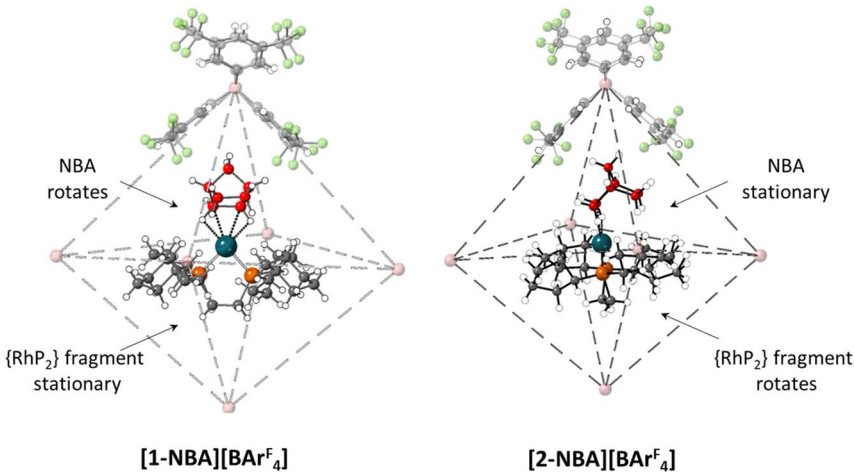

Fig. 10 Packing diagrams contrasting the relative orientations of the NBA and {RhP_2} fragments in **[1-NBA][BAr^F_4]** and **[2-NBA][BAr^F_4]**. The top anion is shown in full along with the B atoms of the other anions within the octahedral array. Carbon atoms of the σ-alkane ligands are highlighted in red.

Returning to the **[1-NBA][BAr^F_4]** system, in the top anion the NBA ligand shows enhanced C–H···F interactions compared to the propane structure. In addition, the more diffuse C–H···π interactions appear energetically more significant and the presence of the C7 methylene bridge in the NBA confers additional interactions that are not possible for propane. The NBA appears to be a particularly good fit to this pocket and its presence has knock-on effects around the anionic octahedral array. The enhanced contribution of C–H···F contacts has already been noted for Eq-2 and Eq-4, however, even for Eq-1 and Eq-3, where the % contributions of the Cy_{inner} and Cy_{outer} cyclohexyl substituents are very similar (and the alkane ligands play a negligible role, Table 2) the overall strength of interaction as gauged *via* the δG^{atom} indices is greater for the NBA system. A range of geometrical parameters were assessed to account for this difference, however no coherent trend could be found. The overall dimensions of the anion octahedron may give some clue: as mentioned in the introduction the Rh cation sits lower down the axial direction in **[1-NBA][BAr^F_4]** while the octahedron of anions itself is slightly compressed along the equatorial axes (B-1···B-3 = 19.26 Å *cf.* 19.94 Å in **[1-propane][BAr^F_4]**; B-2···B-4 = 19.04 Å *cf.* 19.41 Å in **[1-propane][BAr^F_4]**). One possibility is that the octahedral array of anions is more perturbed in **[1-propane][BAr^F_4]** and evidence for this is seen in the wider range of C–H···F anion–anion contacts in this system (1.91–2.75 Å, Fig. 4) whereas these cluster around 2.40 Å in **[1-NBA][BAr^F_4]**. Relating these differences to specific contributions is challenging, however, and most likely the differences in behaviour reflect an accumulation of small effects arising from the subtly different orientations of the cations within each octahedral array of anions, as well as the detailed shape of the octahedra themselves.

Computed BCP $\rho(r)$ values and δG^{atom} indices indicate that the C–H···F interactions provide the strongest non-covalent interactions in these systems and

these two metrics also show a strong correlation (see Fig. S27†). By these measures the C–H···C_{aryl} contacts are less significant; however in these systems such bond paths flag up more diffuse C–H···π interactions that incorporate several atom–atom contributions, the accumulative effect of which is much more significant. While this issue is well-known, and has been addressed in model systems such as the benzene dimer through comparison of QTAIM and NCI plots,[45] the use of the IGMH isosurfaces and quantification *via* $\%\delta G^{atom}$ contributions provide a particularly graphic illustration of these points. The contributions of the more directional C–H···F short contacts are less significant, although the presence of many more of these contacts in **[1-NBA][BAr^F_4]** compared to **[1-propane][BAr^F_4]** may still play a role in the greater stability of the former.

On this note, the recent synthesis of **[1-NBA][S-BAr^F_4]** where S-BAr^F_4 is the Mecking anion in which –SF_5 groups replace the –CF_3 substituents in $[BAr^F_4]^-$ is particularly interesting.[17] This species provides a robust σ-alkane complex that is geometrically analogous to **[1-NBA][BAr^F_4]** in the solid state. Moreover, (unlike its $[BAr^F_4]$ congener) it is completely insoluble in alkane solvents, making it an interesting candidate for a heterogeneous SMOM catalyst. The greater number of C–H···F short contacts in **[1-NBA][S-BAr^F_4]** make it an attractive system for comparison with the current study. This will be the topic of future work, along with the application of high-level quantum mechanical calculations to quantify non-covalent interactions in these systems and benchmark the IGMH approach.

3. Conclusions

Non-covalent interactions around the cationic Rh σ-alkane complexes within the solid state structures of **[1-NBA][BAr^F_4]** and **[1-propane][BAr^F_4]** have been compared. Geometric and QTAIM analyses highlight a greater number of C–H···F contacts around the **[1-NBA]$^+$** cation and the shortest of these correspond to the strongest individual atom–atom non-covalent interactions between the cation and anions in these systems. IGMH plots show the high directionality of these C–H···F interactions, and that these contrast with the more diffuse nature of C–H···π interactions. The accumulative nature of these C–H···π interactions that are distributed over many adjacent atom pairs results in these being more significant in the overall array of cation–anion non-covalent interactions. IGMH δG^{atom} plots provide a particularly useful graphic guide to identifying key non-covalent interactions between the cation and anions. An important contribution from –{C_3H_6}– propylene motifs on both the alkane ligands and the phosphine cyclohexyl substituents is highlighted and these are more significant for **[1-NBA][BAr^F_4]** than **[1-propane][BAr^F_4]**. All measures point to greater non-covalent stabilisation between the cation and anions in **[1-NBA][BAr^F_4]** and this follows the greater stability of this species in the solid state.

Conflicts of interest

There are no conflicts to declare.

Acknowledgements

We thank the EPSRC for funding *via* awards EP/W015498/1 and EP/W015552/1.

References

1 F. M. Chadwick, A. I. McKay, A. J. Martinez-Martinez, N. H. Rees, T. Krämer, S. A. Macgregor and A. S. Weller, *Chem. Sci.*, 2017, **8**, 6014–6029.
2 S. D. Pike and A. S. Weller, *Philos. Trans. R. Soc., A*, 2015, **373**, 20140187.
3 K. A. Reid and D. C. Powers, *Chem. Commun.*, 2021, **57**, 4993–5003.
4 R. H. Crabtree, *Chem. Rev.*, 1985, **85**, 245–269.
5 C. Hall and R. N. Perutz, *Chem. Rev.*, 1996, **96**, 3125–3146.
6 A. S. Weller, F. M. Chadwick and A. I. McKay, in *Advances in Organometallic Chemistry*, ed. P. J. Pérez, Academic Press, 2016, vol. 66, pp. 223–276.
7 For a recent example of the characterisation of σ-alkane complexes in solution see: J. D. Watson, L. D. Field and G. E. Ball, *J. Am. Chem. Soc.*, 2022, **144**, 17622–17629.
8 S. D. Pike, A. L. Thompson, A. G. Algarra, D. C. Apperley, S. A. Macgregor and A. S. Weller, *Science*, 2012, **337**, 1648–1651.
9 S. D. Pike, F. M. Chadwick, N. H. Rees, M. P. Scott, A. S. Weller, T. Krämer and S. A. Macgregor, *J. Am. Chem. Soc.*, 2015, **137**, 820–833.
10 F. M. Chadwick, T. Krämer, T. Gutmann, N. H. Rees, A. L. Thompson, A. J. Edwards, G. Buntkowsky, S. A. Macgregor and A. S. Weller, *J. Am. Chem. Soc.*, 2016, **138**, 13369–13378.
11 A. J. Martínez-Martínez, B. E. Tegner, A. I. McKay, A. J. Bukvic, N. H. Rees, G. J. Tizzard, S. J. Coles, M. R. Warren, S. A. Macgregor and A. S. Weller, *J. Am. Chem. Soc.*, 2018, **140**, 14958–14970.
12 A. I. McKay, A. J. Martínez-Martínez, H. J. Griffiths, N. H. Rees, J. B. Waters, A. S. Weller, T. Krämer and S. A. Macgregor, *Organometallics*, 2018, **37**, 3524–3532.
13 S. K. Furfari, B. E. Tegner, A. L. Burnage, L. R. Doyle, A. J. Bukvic, S. A. Macgregor and A. S. Weller, *Chem.–Eur. J.*, 2021, **27**, 3177–3183.
14 F. M. Chadwick, N. H. Rees, A. S. Weller, T. Krämer, M. Iannuzzi and S. A. Macgregor, *Angew. Chem., Int. Ed.*, 2016, **55**, 3677–3681.
15 A. I. McKay, A. J. Bukvic, B. E. Tegner, A. L. Burnage, A. J. Martinez-Martinez, N. H. Rees, S. A. Macgregor and A. S. Weller, *J. Am. Chem. Soc.*, 2019, **141**, 11700–11712.
16 A. J. Bukvic, A. L. Burnage, G. J. Tizzard, A. J. Martínez-Martínez, A. I. McKay, N. H. Rees, B. E. Tegner, T. Krämer, H. Fish, M. R. Warren, S. J. Coles, S. A. Macgregor and A. S. Weller, *J. Am. Chem. Soc.*, 2021, **143**, 5106–5120.
17 L. R. Doyle, E. A. Thompson, A. L. Burnage, A. C. Whitwood, H. T. Jenkins, S. A. Macgregor and A. S. Weller, *Dalton Trans.*, 2022, **51**, 3661–3665.
18 T. M. Boyd, B. E. Tegner, G. J. Tizzard, A. J. Martínez-Martínez, S. E. Neale, M. A. Hayward, S. J. Coles, S. A. Macgregor and A. S. Weller, *Angew. Chem., Int. Ed.*, 2020, **59**, 6177–6181.
19 A. G. Algarra, A. L. Burnage, M. Iannuzzi, T. Krämer, S. A. Macgregor, R. E. M. Pirie, B. Tegner and A. S. Weller, in *21st Century Challenges in Chemical Crystallography II: Structural Correlations and Data Interpretation*, ed. D. M. P. Mingos and P. R. Raithby, Springer International Publishing, Cham, 2020, pp. 183–228.
20 S. A. Macgregor, T. Krämer, F. M. Chadwick and A. S. Weller, *Helv. Chim. Acta*, 2022, **2023**(106), e202200154.

21 Q. Lu, F. Neese and G. Bistoni, *Phys. Chem. Chem. Phys.*, 2019, **21**, 11569–11577.
22 J. Contreras-García, E. R. Johnson, S. Keinan, R. Chaudret, J.-P. Piquemal, D. N. Beratan and W. Yang, *J. Chem. Theory Comput.*, 2011, **7**, 625–632.
23 T. Lu and Q. Chen, *J. Comput. Chem.*, 2022, **43**, 539–555.
24 M. J. Turner, J. J. McKinnon, S. K. Wolff, D. J. Grimwood, P. R. Spackman, D. Jayatilaka and M. A. Spackman, *CrystalExplorer17*, University of Western Australia, 2017, **https://crystalexplorer.net/**.
25 M. A. Spackman and J. J. McKinnon, *CrystEngComm*, 2002, **4**, 378–392.
26 S. Alvarez, *Dalton Trans.*, 2013, **42**, 8617–8636.
27 R. F. W. Bader, *Atoms in Molecules*, Oxford University Press, 1990.
28 T. A. Keith, *AIMAll*, 2009–2017, **http://aim.tkgristmill.com**.
29 T. Lu and F. Chen, *J. Comput. Chem.*, 2012, **33**, 580–592.
30 W. Humphrey, A. Dalke and K. Schulten, *J. Mol. Graphics*, 1996, **14**, 33–38.
31 E. D'Oria and J. J. Novoa, *CrystEngComm*, 2008, **10**, 423–436.
32 V. R. Thalladi, H. C. Weiss, D. Blaser, R. Boese, A. Nangia and G. R. Desiraju, *J. Am. Chem. Soc.*, 1998, **120**, 8702–8710.
33 P. A. Deck, M. J. Lane, J. L. Montgomery, C. Slebodnick and F. R. Fronczek, *Organometallics*, 2000, **19**, 1013–1024.
34 R. Shukla and D. Chopra, *CrystEngComm*, 2015, **17**, 3596–3609.
35 P. Panini, R. G. Gonnade and D. Chopra, *New J. Chem.*, 2016, **40**, 4981–5001.
36 H. Omorodion, B. Twamley, J. A. Platts and R. J. Baker, *Cryst. Growth Des.*, 2015, **15**, 2835–2841.
37 L. J. L. Häller, M. J. Page, S. A. Macgregor, M. F. Mahon and M. K. Whittlesey, *J. Am. Chem. Soc.*, 2009, **131**, 4604–4605.
38 J. Ran and M. W. Wong, *J. Phys. Chem. A*, 2006, **110**, 9702–9709.
39 M. Nishio, *Phys. Chem. Chem. Phys.*, 2011, **13**, 13873–13900.
40 R. Gopi, N. Ramanathan and K. Sundararajan, *Spectrochim. Acta, Part A*, 2017, **181**, 137–147.
41 R. M. Kumar, M. Elango, R. Parthasarathi, D. Vijay and V. Subramanian, *J. Chem. Sci.*, 2012, **124**, 193–202.
42 C. Lefebvre, G. Rubez, H. Khartabil, J.-C. Boisson, J. Contreras-García and E. Hénon, *Phys. Chem. Chem. Phys.*, 2017, **19**, 17928–17936.
43 C. Lefebvre, H. Khartabil, J.-C. Boisson, J. Contreras-García, J.-P. Piquemal and E. Hénon, *ChemPhysChem*, 2018, **19**, 724–735.
44 A. I. McKay, T. Krämer, N. H. Rees, A. L. Thompson, K. E. Christensen, S. A. Macgregor and A. S. Weller, *Organometallics*, 2017, **36**, 22–25.
45 C. Narth, Z. Maroun, R. A. Boto, R. Chaudret, M.-L. Bonnet, J.-P. Piquemal and J. Contreras-García, in *Applications of Topological Methods in Molecular Chemistry*, ed. E. Alikhani, R. Chauvin, C. Lepetit and B. Silvi, Springer, 2016, vol. 22, pp. 491–527.